








Cite this: *RSC Appl. Interfaces*, 2024,  
1, 471

# Influence of co-reactants on surface passivation by nanoscale hafnium oxide layers grown by atomic layer deposition on silicon†

Sophie L. Pain, <sup>\*,a</sup> Edris Khorani,<sup>a</sup> Anup Yadav, <sup>a</sup> Tim Niewelt,<sup>abc</sup>  
Antonio Leimenstoll,<sup>b</sup> Brendan F. M. Healy, <sup>a</sup> Marc Walker, <sup>d</sup> David Walker, <sup>d</sup>  
Nicholas E. Grant <sup>a</sup> and John D. Murphy <sup>a</sup>

Hafnium oxide thin films have attracted considerable interest for passivation layers, protective barriers, and anti-reflection coatings. Atomic layer deposition offers a route to produce conformal films at the nanometre scale, but there is a lack of clarity over how the growth conditions affect the film properties. Here we present a study into the role of different atomic layer deposition co-reactants ( $O_2$  plasma,  $O_3$  and  $H_2O$ ) in the growth of  $HfO_x$  on n-type silicon from a tetrakis(dimethylamido)hafnium (TDMAH) precursor followed by post-deposition annealing (up to 500 °C). Through X-ray diffraction and X-ray photoelectron spectroscopy, we demonstrate variations in film composition, stoichiometry and crystallinity with co-reactant. Depth profiling conducted with X-ray photoelectron spectroscopy reveals differences in composition between the  $HfO_x$  surface and the  $HfO_x/Si$  interface. We also determine differences in fixed charge density and chemical passivation through photoconductance decay measurements and Kelvin probe analysis. We find surface recombination velocities (SRVs)  $<10\text{ cm s}^{-1}$  are possible for  $HfO_x$  films, with the best passivation achieved for  $H_2O$ -based  $HfO_x$  (SRVs as low as  $\sim 5\text{ cm s}^{-1}$ ). With TDMAH as a hafnium precursor, we show that neither co-reactant choice nor annealing environment influence the resulting charge polarity.

Received 25th October 2023,  
Accepted 6th December 2023

DOI: 10.1039/d3lf00210a

rsc.li/RSCApplInter

## Introduction

Surface passivation aims to minimise unwanted recombination of charge carriers in semiconductors which, in the case of silicon, is key to improving solar cell efficiency. Passivation arises from both chemical and field effects, with the former involving termination of dangling bonds at the semiconductor surface, and the latter involving surface charges which can repel charge carriers. Deposition of dielectrics is an established passivation strategy,<sup>1</sup> with atomic layer deposition (ALD) being commonly used. ALD is based

on sequential self-terminating reactions, and offers thickness control with atomic layer precision, as well as uniform and conformal deposition.<sup>2–5</sup> Deposition process temperature, pressure, duration, and other parameters play a key role in achieving the desired film properties.<sup>5</sup> ALD-grown films are usually annealed *ex situ* to “activate” the passivation, with the passivation level strongly affected by the post-deposition annealing temperature due to variations in chemical and field effects.<sup>6,7</sup>

The chemical reaction step of ALD can be conducted either thermally or enhanced by the presence of a plasma.<sup>4</sup> In thermal ALD, one of the precursors is typically a gas such as  $O_2$ , or a vapour such as  $H_2O$  or  $O_3$ . During plasma-enhanced ALD (PE-ALD), a plasma is generated from a gas (such as  $O_2$ ,  $N_2$  or  $H_2$ ), and the substrate surface is exposed to the species generated.

Recent studies have identified  $HfO_x$  as a promising passivating layer.<sup>8–14</sup> ALD-grown  $HfO_x$  passivation studies have achieved surface recombination velocities (SRVs)  $<10\text{ cm s}^{-1}$  (compared to  $<2\text{ cm s}^{-1}$  for thermal  $SiO_2$  and  $<1\text{ cm s}^{-1}$  for ALD  $Al_2O_3$ )<sup>1,15,16</sup> for films 10–20 nm thick.<sup>8–14</sup> In addition to its potential as an insulating silicon passivation layer, the electronic properties of  $HfO_x$  make it a candidate for inclusion within passivating contact structures, either as a

<sup>a</sup> School of Engineering, University of Warwick, Coventry, CV4 7AL, UK.E-mail: [sophie.l.pain@warwick.ac.uk](mailto:sophie.l.pain@warwick.ac.uk)<sup>b</sup> Fraunhofer Institute for Solar Energy Systems ISE, Heidenhofstraße 2, 79110 Freiburg, Germany<sup>c</sup> Chair for Photovoltaic Energy Conversion, Institute for Sustainable Systems Engineering, University of Freiburg, Emmy-Noether-Straße 2, 79110 Freiburg, Germany<sup>d</sup> Department of Physics, University of Warwick, Coventry, CV4 7AL, UK† Electronic supplementary information (ESI) available: Thickness measurements and optical characterisation of the deposited layers, XPS data corresponding to depth profiling of  $O_2^-$ ,  $O_3^-$  and  $H_2O-HfO_x$ , and representative signal fitting. See DOI: <https://doi.org/10.1039/d3lf00210a>

hole-selective contact<sup>17,18</sup> or as an interlayer.<sup>19</sup> Beyond silicon passivation,  $\text{HfO}_x$  has been extensively researched by the (micro)electronics industry for applications in transistors and capacitors<sup>20,21</sup> due to its high dielectric constant, and as a protective barrier layer, due to the impressive chemical resistance of  $\text{HfO}_x$  to etchants such as  $\text{HF}$ .<sup>22</sup>

Although there has been considerable interest in ALD-grown  $\text{HfO}_x$ , there is a lack of consistency in film properties reported in the literature, as demonstrated in Table 1 of ref. 18. This is particularly evident when considering  $\text{HfO}_x$  charge polarity, which has been reported as being both positive and negative,<sup>8–14</sup> even for films processed under very similar conditions. This inconsistency could arise from several process parameters – such as hafnium precursor, co-reactant, deposition temperature and pressure, and post-deposition processing. To date, investigations have been conducted into the impact of varying co-reactant (mainly  $\text{H}_2\text{O}$  and  $\text{O}_3$ ) with tetrakis(ethylmethanido)hafnium (TEMAH), hafnium tetrachloride ( $\text{HfCl}_4$ ) and tetrakis(dimethylamido)hafnium (TDMAH) precursors,<sup>11,23,24</sup> and into the effect of changing precursor while maintaining co-reactant.<sup>25</sup> Multiple parameters were varied within these studies, making it difficult to ascribe changes in film properties and performance to any specific effect. Additionally, the inter- and intra-precursor variability in film properties suggests that conclusions drawn from one study may not necessarily be applicable to another investigation with different parameters.

Here we present a systematic study into the impact of co-reactants on film properties of  $\text{HfO}_x$  grown with a TDMAH precursor. Oxidant choice can affect electrical properties, impurities, refractive indices, and morphology<sup>26</sup> and hence we investigate three co-reactants: remote oxygen plasma (with resultant films hereafter denoted  $\text{O}_2\text{-HfO}_x$ ), ozone ( $\text{O}_3\text{-HfO}_x$ ) and water ( $\text{H}_2\text{O-HfO}_x$ ). Post-deposition annealing conditions, such as annealing environment, are another key parameter varied in the literature,<sup>27</sup> and we assess the impact of four annealing environments (air, forming gas,  $\text{O}_2$  and  $\text{N}_2$ ) on resulting passivation quality.

## Results and discussion

### Structural properties

To allow comparison between films grown from different co-reactants, a constant number of ALD cycles (200) was used for all samples discussed in this study. We have previously determined that 200 ALD cycles of  $\text{O}_2\text{-HfO}_x$  results in a 26 nm thick film,<sup>22</sup> and we find similar film thicknesses with  $\text{H}_2\text{O-HfO}_x$  and  $\text{O}_3\text{-HfO}_x$  of 25 and 23 nm, respectively. Film thickness can play a significant role in  $\text{HfO}_x$  film properties, notably with passivation when films are very thin,<sup>19</sup> although the difference is lesser at greater thicknesses. These films are of a very similar thickness at a thickness level where passivation is not strongly thickness dependent, ensuring that comparison between film types is meaningful. Thickness measurements for each film type, and derived growth rates per ALD cycle are shown in Fig. S1(a) in the ESI.†

Much of the behaviour of hafnium oxide, such as its chemical resistance<sup>22</sup> and optical properties (shown in Fig. S1(b)†),<sup>28</sup> has been attributed to crystallisation. We have previously investigated extensively the crystallisation behaviour of  $\text{O}_2\text{-HfO}_x$  as a function of annealing temperature,<sup>6,22</sup> and have determined an amorphous-to-crystalline phase transition at 275–325 °C. Our prior work found that good passivation quality was achieved following annealing after this crystallisation point, whether this is as a result of crystallisation is as yet unclear. To assess whether there is any difference in crystallinity and this phase transition, we performed grazing-incidence X-ray diffraction (GI-XRD) on all film types, both in the as-deposited state and after annealing in air at ~450 °C. The resulting GI-XRD patterns are presented in Fig. 1(a)–(c) for  $\text{O}_2\text{-HfO}_x$ ,  $\text{H}_2\text{O-HfO}_x$  and  $\text{O}_3\text{-HfO}_x$ , respectively. Irrespective of co-reactant, all three  $\text{HfO}_x$  film types are amorphous on deposition. The low intensity features seen in the  $2\theta$  range of 50–60° of each XRD pattern can be attributed to the (311) plane of the underlying c-Si (100) substrate.<sup>29</sup> Following annealing at ~450 °C,  $\text{O}_2\text{-HfO}_x$  and  $\text{H}_2\text{O-HfO}_x$  undergo a clear phase transition to monoclinic, although  $\text{O}_3\text{-HfO}_x$  does not, remaining amorphous. It is as yet unclear why  $\text{O}_3\text{-HfO}_x$  appears to have different crystallisation behaviour than its  $\text{O}_2\text{-}$  and  $\text{H}_2\text{O-HfO}_x$  counterparts.

### Chemical properties

To explore the origins of this differing behaviour, ~25 nm films were subsequently characterised *via* X-ray photoelectron spectroscopy (XPS). Survey scans for each film are shown in Fig. 1(d), with core levels labelled. All XPS spectra were calibrated to the C 1s core level. The survey scans are dominated by Hf and O signals. No evidence of the underlying Si substrate is detectable, as the film thickness far exceeds the photoelectron sampling depth (~10 nm).<sup>30,31</sup>

There are no significant differences in the survey scans for each material, however closer inspection of the electronic core levels *via* high resolution scans reveals some variations in composition, both between film types and at each stage of depth profiling. Relative atomic concentrations of each species present were determined as a function of depth into the material. The Hf 4f and O 1s core levels were used to determine the stoichiometry of the  $\text{HfO}_x$  films as a function of depth, and Si 2p was used for silicon (*i.e.*, identifying when we have milled to the  $\text{HfO}_x/\text{Si}$  interface). Three clear regions are evident from this depth profiling – surface/near-surface, bulk dielectric, and the  $\text{HfO}_x/\text{Si}$  interface, as annotated in Fig. 1(e). The Hf 4f and Si 2p signals allow determination of an approximate milling rate. Once sufficient  $\text{HfO}_x$  overlayer had been milled away to allow detection of the underlying Si substrate, film thicknesses could be determined *via* the thickogram method.<sup>32</sup> These thickness are presented in Fig. 1(f).

For  $\text{O}_2\text{-HfO}_x$  and  $\text{H}_2\text{O-HfO}_x$ , this required cumulative milling of ~2500 s, at which point hafnium oxide thicknesses



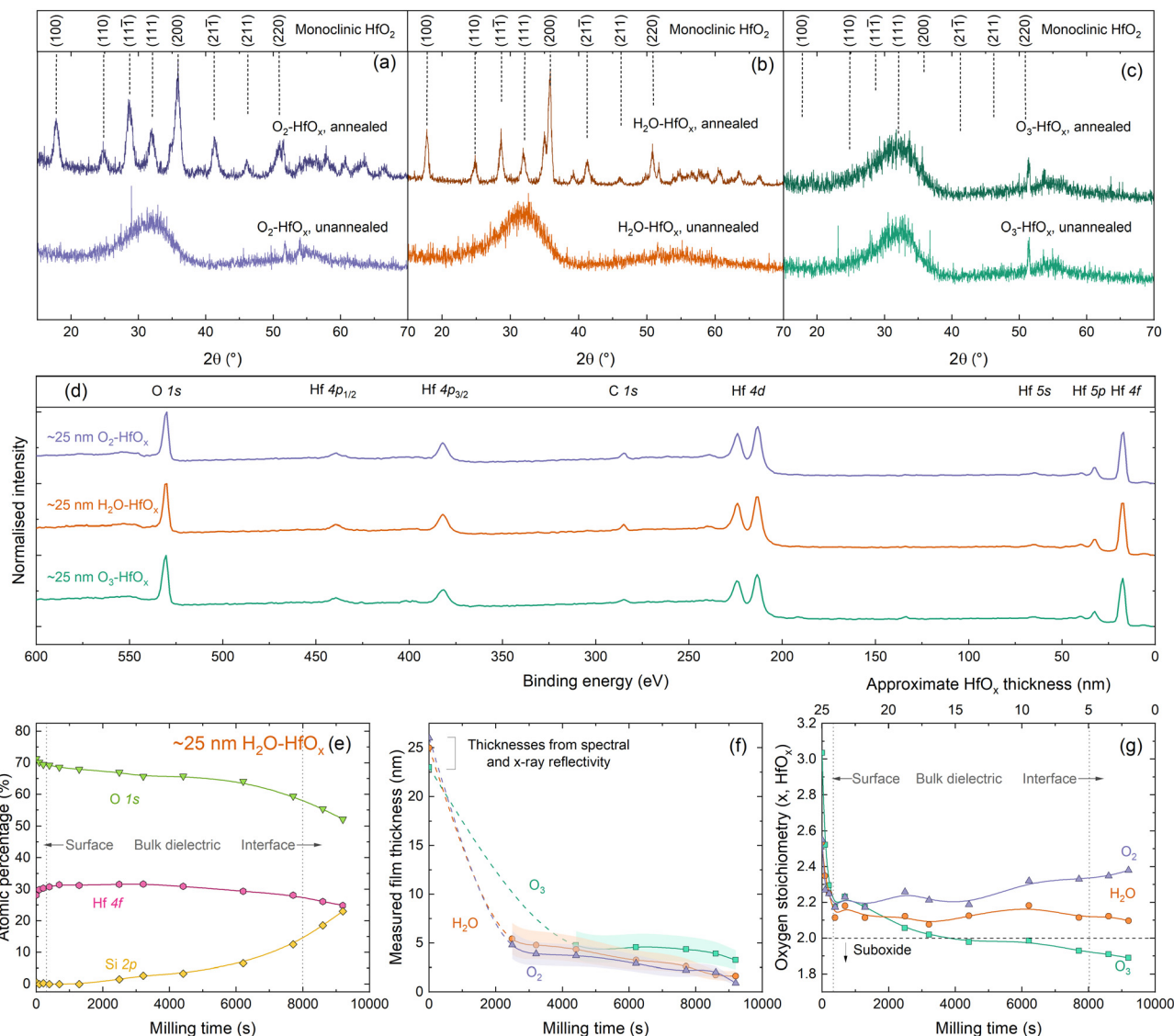


**Fig. 1** (a) GI-XRD patterns, using Cu  $K_{\alpha 1/2}$ , taken from polished silicon wafers coated with (a)  $\text{O}_2\text{-HfO}_x$ , (b)  $\text{H}_2\text{O-HfO}_x$  and (c)  $\text{O}_3\text{-HfO}_x$  as deposited (unannealed) or following annealing at 450–475 °C for 30 min in air. The sharp signals visible at  $2\theta = \sim 27^\circ$  for unannealed  $\text{O}_2\text{-HfO}_x$  and  $2\theta = \sim 23^\circ$  and  $\sim 36^\circ$  for unannealed  $\text{O}_3\text{-HfO}_x$  are measurement artefacts. Patterns are vertically offset for clarity.  $\text{O}_2\text{-HfO}_x$  GI-XRD data (purple lines) were previously published in ref. 6. Main crystallographic planes, corresponding to monoclinic  $\text{HfO}_2$ , are labelled above.<sup>33</sup> (d) XPS Survey scans for  $\sim 25$  nm  $\text{O}_2\text{-HfO}_x$  (purple),  $\text{O}_3\text{-HfO}_x$  (green) and  $\text{H}_2\text{O-HfO}_x$  (orange) after annealing at 450 °C. All XPS spectra were calibrated to the C 1s core level. Core levels are labelled. Survey scan was collected prior to milling with  $\text{Ar}^+$ . (e) Atomic concentrations (%) determined via XPS for Hf (pink circles), O (green triangles) and Si (yellow diamonds, determined from intensity of signal at a binding energy of  $\sim 99$  eV) as a function of milling time for  $\text{H}_2\text{O-HfO}_x$ , shown for demonstration purposes. (f) Determined film thickness via the thickogram method<sup>32</sup> for  $\text{O}_2\text{-HfO}_x$ ,  $\text{H}_2\text{O-HfO}_x$  and  $\text{O}_3\text{-HfO}_x$  (purple triangles, orange circles and green squares, respectively) as a function of XPS milling time. Initial thicknesses determined via X-ray or spectral reflectivity. Connections between points serve as a guide to the eye. Shaded region corresponds to the relative uncertainty of determined thickness. (g)  $\text{HfO}_x$  stoichiometry as a function of milling time.

of 4.8 and 5.4 nm were determined, respectively.  $\text{O}_3\text{-HfO}_x$  required  $\sim 4400$  s milling to thin the hafnium oxide layer sufficiently (to 4.8 nm) to detect the Si substrate. Once the substrate was detectable, milling rates of  $\sim 7 \times 10^{-4}$ ,  $6 \times 10^{-4}$  and  $5 \times 10^{-4}$  nm  $\text{s}^{-1}$  were determined from the measured dataset for  $\text{O}_2\text{-HfO}_x$ ,  $\text{H}_2\text{O-HfO}_x$  and  $\text{O}_3\text{-HfO}_x$ , respectively. Slight variations in milling rates are not unexpected, and can arise from compositional variations and differential sputtering, although the differences in milling rate observed

here are relatively small, within the same order of magnitude.

From determined atomic percentages, the oxygen stoichiometry  $x$  for  $\text{HfO}_x$  can be inferred from  $1/([\text{Hf}]/[\text{O}])$ . The whole of the O 1s and Hf 4f<sub>7/2</sub> signal are used in this calculation, rather than any deconvoluted contribution, to facilitate comparison between different film types.

We note that there can be additional contributions to [O] which are not related to Hf–O bonds. Near the sample

surface, some of the O 1s signal will be related to organic hydrocarbon contamination, hence at in this region [O] is likely overestimated. Furthermore, near the dielectric-silicon interface,  $\text{SiO}_x$  interlayers are known to form under these conditions<sup>12</sup> and could also skew determined [O]. Characterisation of this interfacial oxide by XPS is challenging, as the O 1s signal will comprise overlapping contributions from both Si-O and Hf-O bonding, in addition to the potential effects of sputter damage and differential sputtering. Hence, the whole [O] signal is considered, rather than any sub-component. Oxygen stoichiometries for all three films as a function of milling time/approximate film thickness are plotted in Fig. 1(g).

XPS analysis of the initial (un-milled) film shows an oxygen-rich film in each case, with  $x = 2.3$  for  $\text{O}_2\text{-HfO}_x$  and  $\text{H}_2\text{O-HfO}_x$  and  $x = 2.5$  for  $\text{O}_3\text{-HfO}_x$ . Following  $\sim 400$  s of milling,  $x$  decreases for  $\text{O}_2\text{-HfO}_x$  and  $\text{H}_2\text{O-HfO}_x$  to 2.1–2.2 and remains in this range with increased milling time. Following 9200 s of milling,  $x$  increases once more to  $\sim 2.4$  and  $\sim 2.1$  for  $\text{O}_2\text{-HfO}_x$  and  $\text{H}_2\text{O-HfO}_x$ , respectively. The initial decrease in  $x$  corresponds to a reduction in [O], likely related to removal of sample surface hydrocarbon contamination.

With milling time, there is a change in determined stoichiometry for  $\text{O}_3\text{-HfO}_x$ , which appears to become less oxygen-rich with milling time (depth). It is important to highlight that this change could arise from the milling process itself—the considerable difference in atomic mass between O and Hf would result in differential sputtering,

whereby O is removed more readily than Hf, hence affecting the [Hf]/[O] ratio. The observed  $x$  reduces to  $\sim 2.2$  in the first  $\sim 500$  s, but continues to decrease monotonically with increased milling, eventually forming hafnium sub-oxide with  $x = 1.9$ .

The Hf 4f peak observed here can be deconvoluted into several contributing signals. Fig. 2 presents fitted spectra for both unmilled and milled  $\text{O}_2\text{-HfO}_x$ ,  $\text{O}_3\text{-HfO}_x$ , and  $\text{H}_2\text{O-HfO}_x$ , respectively. The unmilled spectra are largely similar, although two small contributions are visible at  $\sim 18$  and  $\sim 19$  eV in the spectra of  $\text{O}_3\text{-HfO}_x$ . These peaks, corresponding to Hf 4f<sub>7/2</sub> and Hf 4f<sub>5/2</sub> respectively, may arise from surface contamination, as Zrinski *et al.* attribute signals at this binding energy to hafnium phosphate.<sup>34</sup> The definitive source of this impurity is unclear, but it may have arisen from annealing in a tube furnace which had previously been used for phosphorous diffusions. Importantly, these signals are lost after three milling steps, indicating that this is localised to the surface, rather than distributed throughout the film, we do not consider it influential for film performance.

Within the Hf 4f signal, the most prominent contributions are the 4f<sub>5/2</sub> and 4f<sub>7/2</sub> oxide signals, which also dominate the corresponding region of the milled XPS spectra. After extended milling, hafnium suboxide peaks (at  $\sim 18$  and  $\sim 16$  eV for Hf 4f<sub>5/2</sub> and Hf 4f<sub>7/2</sub>, respectively) and metallic Hf peaks (at  $\sim 17$  and  $\sim 14.6$  eV for Hf 4f<sub>5/2</sub> and Hf 4f<sub>7/2</sub>, respectively) are visible. The appearance of a metallic Hf

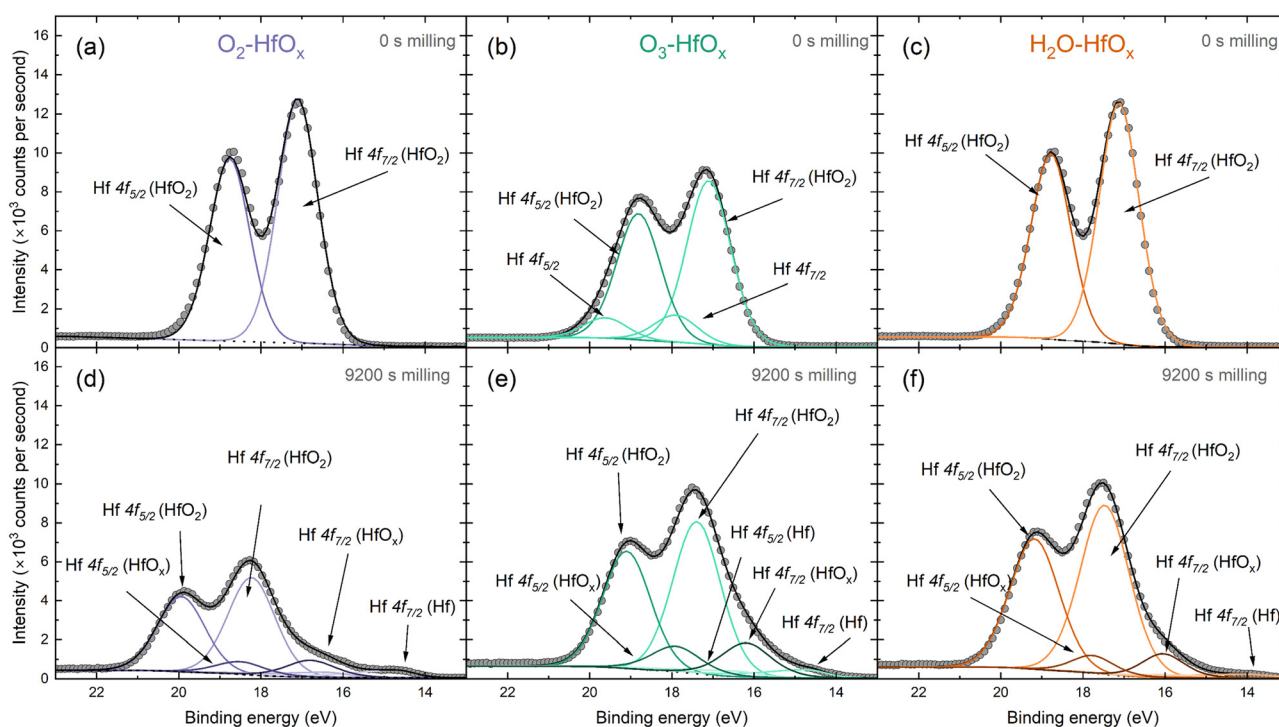


**Fig. 2** Peak deconvolution of  $\text{HfO}_x$  4f XPS signal, with Hf 4f<sub>5/2</sub> and Hf 4f<sub>7/2</sub> contributions identified from  $\text{O}_2\text{-HfO}_x$ ,  $\text{O}_3\text{-HfO}_x$  and  $\text{H}_2\text{O-HfO}_x$  before milling (a–c) and following 9200 s of  $\text{Ar}^+$  milling (d–f). The grey circles are recorded data and dotted/dashed/solid lines correspond to fitted data. Fitting and chemical state analysis were supported by the NIST XPS database.<sup>35</sup>



signal as we near the interface could be linked to a change in interfacial composition, a product of differential sputtering or sputter damage.

Fig. S2 in the ESI† allows comparison of all three film types at each milling depth. In all cases, there is a shift in the position of both the Hf  $4f_{5/2}$  and the Hf  $4f_{7/2}$  oxide contributions to higher binding energies. This shift in Hf  $4f$  position suggests a change in bonding configuration, with positive shifts generally associated with oxidation. Of these shifts, the most prominent are that of  $O_2$ -HfO<sub>x</sub> and H<sub>2</sub>O-HfO<sub>x</sub>, with a shift towards a binding energy of  $\sim 20$  eV for the Hf  $4f_{5/2}$  peak, whereas  $O_3$ -HfO<sub>x</sub> the Hf  $4f_{5/2}$  peak only shifts to  $\sim 19$  eV.

### Passivation properties

A key metric in silicon passivation is the charge carrier lifetime in a passivated substrate. From this we can derive more interface-specific parameters such as surface recombination velocity (SRV) and dark surface saturation current  $J_{0s}$ . Following film deposition, and after annealing in air for 30 min at temperatures 300–500 °C, effective lifetimes were recorded *via* photoconductance decay. Effective lifetimes were extracted at an excess carrier density of  $1 \times 10^{15} \text{ cm}^{-3}$  and are plotted in Fig. 3(a). Corresponding injection dependent lifetime curves can be found in Fig. 3(b)–(d) for  $O_2$ -HfO<sub>x</sub>, H<sub>2</sub>O-HfO<sub>x</sub> and  $O_3$ -HfO<sub>x</sub>, respectively.

At all annealing temperatures studied, H<sub>2</sub>O-HfO<sub>x</sub> exhibits the most promising passivation quality, with single-side  $J_{0s}$  values  $< 20 \text{ fA cm}^{-2}$  possible at all annealing temperatures, consistent with studies of thermal deposition of Al<sub>2</sub>O<sub>3</sub> on n-type silicon.<sup>16</sup>  $O_2$ -HfO<sub>x</sub> and  $O_3$ -HfO<sub>x</sub> initially passivate poorly and require an ‘activation’ anneal at around 400 °C for reasonable passivation (minimum  $J_{0s}$  achieved of 33 and 71 fA cm<sup>-2</sup> for  $O_2$ -HfO<sub>x</sub> and  $O_3$ -HfO<sub>x</sub>, respectively) to be realised.

The best passivation quality for  $O_3$ -HfO<sub>x</sub> (albeit less competitive than the other films) occurs following annealing at a temperature (400 °C) at which, based on the XRD results in Fig. 1, the film is still amorphous, suggesting that crystallisation is not a pre-requisite for passivation, consistent with our prior work on ultra-thin hafnium oxide films.<sup>18</sup> Above this temperature, the passivation quality of  $O_3$ -HfO<sub>x</sub> gradually degrades – this decline is likely due to degradation of the surface passivation rather than the bulk, as there is no evidence of degradation in samples of the same substrate type with the other two HfO<sub>x</sub> films. We have previously verified the stability of the substrate bulk carrier lifetime with  $O_2$ -HfO<sub>x</sub> passivation of nominally identical substrates using a superacid-based re-passivation method.<sup>6</sup>

Importantly, films grown with all three co-reactants require annealing at 350–425 °C to allow for millisecond-level effective lifetimes (SRVs at  $1 \times 10^{15} \text{ cm}^{-3} < 10 \text{ cm s}^{-1}$ ) to be achieved.  $\sim 100 \mu\text{s}$  effective lifetimes (equivalent to an average SRV of  $76.7 \text{ cm s}^{-1}$ , an order of magnitude lower than recent reports of H<sub>2</sub>O-based HfO<sub>x</sub> (ref. 36)) were

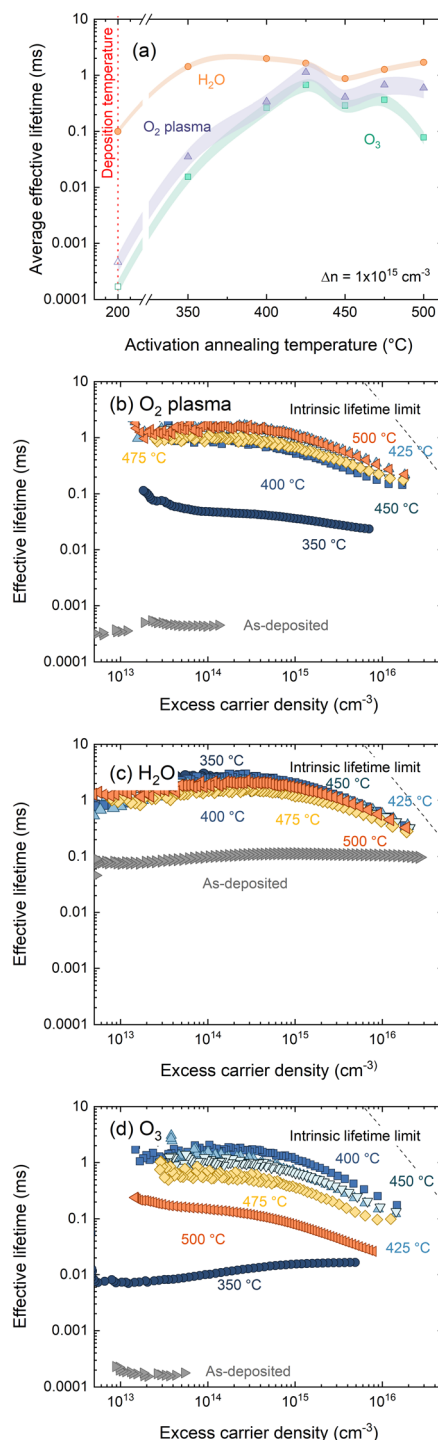


**Fig. 3** (a) Effective lifetimes extracted at  $\Delta n = 1 \times 10^{15} \text{ cm}^{-3}$  for  $O_2$ -HfO<sub>x</sub> (purple triangles),  $O_3$ -HfO<sub>x</sub> (green squares) and H<sub>2</sub>O-HfO<sub>x</sub> (orange circles), as deposited and after annealing in air at temperatures 350–600 °C. Samples were  $\sim 150 \mu\text{m}$ , (100), 5  $\Omega \text{ cm}$ , n-type Cz-silicon. Multiple samples were characterised following annealing at 400 °C ( $O_2$ -HfO<sub>x</sub>,  $O_3$ -HfO<sub>x</sub>), 450 °C ( $O_2$ -HfO<sub>x</sub>, H<sub>2</sub>O-HfO<sub>x</sub>,  $O_3$ -HfO<sub>x</sub>) and 500 °C ( $O_2$ -HfO<sub>x</sub>), with the lifetime values presented herein an average of those samples. The shaded regions correspond to the experienced variation between samples. The as-deposited values at  $\Delta n = 1 \times 10^{15} \text{ cm}^{-3}$  for  $O_2$ -HfO<sub>x</sub> and  $O_3$ -HfO<sub>x</sub>, indicated with open triangles and squares, respectively, are estimated by the Sinton software. Injection dependent lifetime curves for (b)  $O_2$ -HfO<sub>x</sub>, (c) H<sub>2</sub>O-HfO<sub>x</sub> and (d)  $O_3$ -HfO<sub>x</sub> annealed in air at temperatures 350–600 °C and as-deposited. Also shown in each case is the effective lifetime limit.<sup>40</sup>



recorded for as-deposited  $\text{H}_2\text{O}-\text{HfO}_x$  – which is orders of magnitude better than those determined for as-deposited  $\text{O}_3-\text{HfO}_x$  and  $\text{O}_2-\text{HfO}_x$ . Indeed,  $\text{O}_3-\text{HfO}_x$  and  $\text{O}_2-\text{HfO}_x$  require annealing at 400 °C to reach the same level of passivation. The increase in effective lifetime at  $1 \times 10^{15} \text{ cm}^{-3}$  for  $\text{O}_2-\text{HfO}_x$  and  $\text{O}_3-\text{HfO}_x$  following annealing at this temperature coincides with a change in injection dependence, as evident from Fig. 3(b) and (d). The passivation quality of  $\text{H}_2\text{O}-\text{HfO}_x$  can be improved with a similar activation anneal of  $\leq 350$  °C, lower than reported previously.<sup>11</sup>

An important property of dielectrics is the character of the fixed charges, the undefined nature of which in  $\text{HfO}_x$  has attracted much attention.<sup>9–11,25,27,37</sup> Consequently, it is necessary to understand the effects of any charge present in the ultra-thin films with changing deposition co-reactant. Charge polarity can be assessed from the direction of shift under illumination when making surface photovoltage (SPV) measurements using a Kelvin probe setup, where negative SPV corresponds to negative charge and *vice versa*.<sup>38,39</sup> KP analysis in Fig. 4(a) shows that all the  $\text{HfO}_x$  films are negatively charged, irrespective of ALD co-reactant. Consistent charge polarity with different co-reactants concurs with the work of Park *et al.* on  $\text{HfCl}_4$ -based  $\text{HfO}_x$ , although they observe positive charges.<sup>24</sup> Negative SPV is observed prior to any annealing steps, indicating the negative charge is present from deposition, rather than induced on annealing, as has previously been suggested.<sup>11</sup>

SPV values are similar for each film type (within one standard deviation) in all cases. Beyond SPV, contact potential difference (used in determination of SPV) can provide additional insight into material properties, with greater CPD corresponding to more highly charged films. Whereas the differences in SPV between the films plotted in Fig. 4(b) were within experimental variation, the same cannot be said for  $\text{CPD}_{\text{dark}}$  plotted in Fig. 4(c). Following deposition,  $\text{CPD}_{\text{dark}}$  differs for each co-reactant, with a separation of  $\sim 500$  mV in  $\text{CPD}_{\text{dark}}$  between each  $\text{HfO}_x$  film type ( $-800$ ,  $-300$ ,  $200$  mV for  $\text{HfO}_x-\text{H}_2\text{O}$ ,  $\text{HfO}_x-\text{O}_3$  and  $\text{HfO}_x-\text{O}_2$ ,

respectively). With annealing, this difference reduces, with all film types reaching a  $\text{CPD}_{\text{dark}}$  of  $\sim -100$ – $300$  mV, irrespective of co-reactant or annealing temperature.

The magnitude of SPV can be indicative of the quantity of charge present but results can be highly variable and dependent on both material properties and surface defects.<sup>14,41</sup> Thus, positive corona charging was used to characterize the negative fixed charge ( $Q_{\text{fixed}}$ ) present in  $\text{HfO}_x$  grown by each method more reliably. This is based on adding extrinsic charge  $Q_{\text{corona}}$  to counteract the intrinsic  $Q_{\text{fixed}}$ .<sup>42</sup> Corona charging also allows an estimate of the level of chemical passivation at the interface from  $\tau_{\text{min}}$ , which is the lowest effective lifetime that is expected to indicate the point at which  $Q_{\text{fixed}}$  is negated by  $Q_{\text{corona}}$ , leaving only chemical passivation and hence a proxy for interface trap density  $D_{\text{it}}$ .<sup>43</sup> Following neutralisation of fixed charge, applying further extrinsic positive charge causes an increase in measured effective lifetime, as the applied charge provides field effect passivation.

The result of such investigation of the differently deposited layers annealed at varied temperatures is presented in Fig. 5. The effect of successive corona charging on measured effective lifetime is demonstrated in Fig. 6(a) for  $\text{O}_2-\text{HfO}_x$ ,  $\text{O}_3-\text{HfO}_x$  and  $\text{H}_2\text{O}-\text{HfO}_x$  annealed at 450 °C. From this procedure, values for  $Q_{\text{corona}}$  ( $-Q_{\text{fixed}}$ ) and  $\tau_{\text{min}}$  can be extracted. These parameters are summarised in Fig. 5(b) and (c), respectively. The recovery of measured effective lifetime past the minimum point in Fig. 5(a) is more pronounced for  $\text{O}_2$  and  $\text{H}_2\text{O}-\text{HfO}_x$  than for  $\text{O}_3-\text{HfO}_x$ . Corona charging having minimal impact on effective lifetime, has been attributed to charge leakage.<sup>6,7,19,44</sup> As such, we speculate that the lack of improvement in  $\text{O}_3-\text{HfO}_x$  lifetime could be attributed to this, noting we did not characterise charge leakage in this study.

$\text{H}_2\text{O}-\text{HfO}_x$  has similar values of both  $Q_{\text{fixed}}$  and  $\tau_{\text{min}}$  at all studied annealing temperatures, demonstrating that in this temperature range both field- and chemical-effect passivation are relatively constant. There is a slight increase in  $Q_{\text{fixed}}$  between 350–400 °C, but at all temperatures  $Q_{\text{fixed}}$  is  $-2 \times 10^{12}$  to

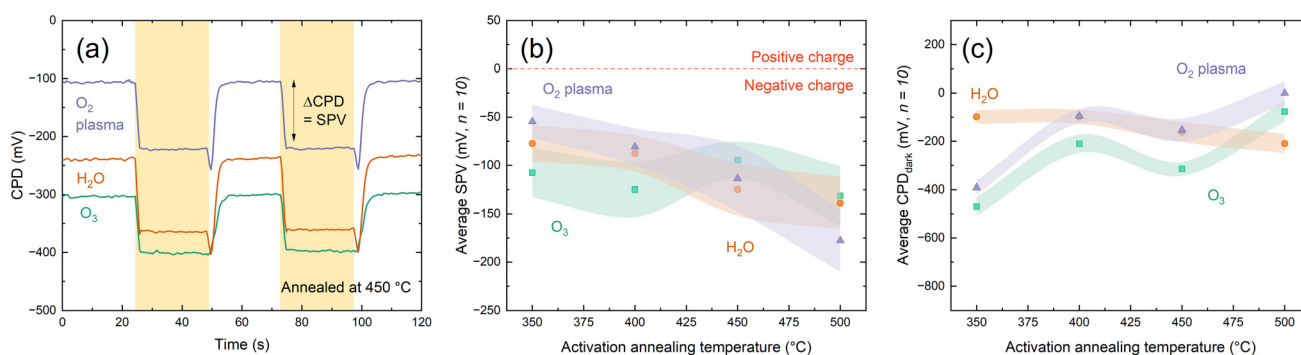
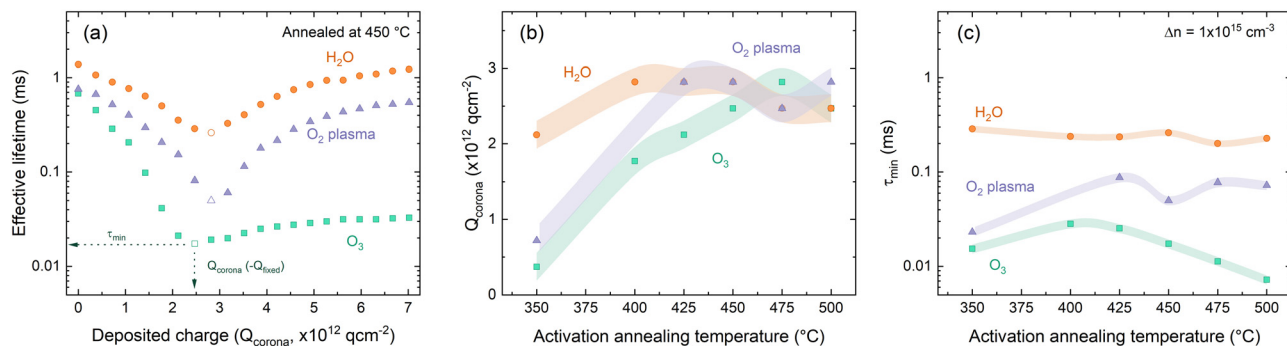


Fig. 4 (a) Representative surface photovoltage measurement for  $\text{O}_2-\text{HfO}_x$  (purple),  $\text{H}_2\text{O}-\text{HfO}_x$  (orange) and  $\text{O}_3-\text{HfO}_x$  (green) after annealed in air at 450 °C. The yellow shaded regions correspond to periods of illumination. Surface photovoltage (b) and  $\text{CPD}_{\text{dark}}$  (c) for  $\text{O}_2-\text{HfO}_x$  (purple triangles),  $\text{O}_3-\text{HfO}_x$  (green squares) and  $\text{H}_2\text{O}-\text{HfO}_x$  (orange circles), as deposited and annealed in air at temperatures 350–600 °C. In both cases, the plotted value is the average of ten measurements, and the shaded region corresponds to the standard deviation of these values.





**Fig. 5** (a) Effective lifetime as a function of  $Q_{\text{corona}}$  for  $\text{O}_2\text{-HfO}_x$  (purple triangles),  $\text{O}_3\text{-HfO}_x$  (green squares) and  $\text{H}_2\text{O-HfO}_x$  (orange circles), annealed in air at 450 °C. The datapoint at which  $Q_{\text{fixed}}$  and  $\tau_{\text{min}}$  are extracted is indicated in each case.  $Q_{\text{corona}}$  (b) and  $\tau_{\text{min}}$  (c) for  $\text{O}_2\text{-HfO}_x$  (purple triangles),  $\text{O}_3\text{-HfO}_x$  (green squares) and  $\text{H}_2\text{O-HfO}_x$  (orange circles), annealed in air at temperatures 350–600 °C. In both cases, the shaded region corresponds to the relative uncertainty of the measurement: (b)  $Q_{\text{corona}}$  of  $1.85 \times 10^{11} \text{ q cm}^{-2}$ , 50% of  $Q_{\text{corona}}$  deposited in each step and (c) 8% under short flash conditions, and 11% under long flash conditions.<sup>46</sup>

$-3 \times 10^{12} \text{ q cm}^{-2}$  (cf.,  $\sim 10^{11} \text{ q cm}^{-2}$  previously reported for  $\text{H}_2\text{O-HfO}_x$  grown with this precursor,<sup>11</sup> and  $\sim 10^{12}$  to  $10^{13} \text{ q cm}^{-2}$  for the more conventional  $\text{Al}_2\text{O}_3$ ).<sup>7,15,16</sup> The trends observed with  $\text{H}_2\text{O-HfO}_x$  differ from  $\text{HfO}_x$  grown with other co-reactants. As shown in Fig. 5(b),  $\text{O}_3\text{-HfO}_x$  annealed at 350 °C has  $Q_{\text{fixed}} \leq -7 \times 10^{11} \text{ q cm}^{-2}$ , a value which increases monotonically with annealing temperature up to 475 °C at which point there is a slight decline. Increasing  $Q_{\text{fixed}}$  with annealing temperature has previously been observed for  $\text{O}_2\text{-HfO}_x$ ,<sup>6</sup>

an observation which was correlated with film crystallisation at similar temperatures. As  $\text{O}_3\text{-HfO}_x$  does not appear to crystallise in this temperature range, it follows that the increase in charge magnitude is not connected with  $\text{HfO}_x$  crystallisation.

In terms of  $\tau_{\text{min}}$ , plotted in Fig. 5(c) at all annealing temperatures,  $\text{O}_3\text{-HfO}_x$  has the lowest levels of chemical passivation of the three materials studied. The greatest  $\tau_{\text{min}}$  (i.e., best chemical passivation) is observed at 400–425 °C,

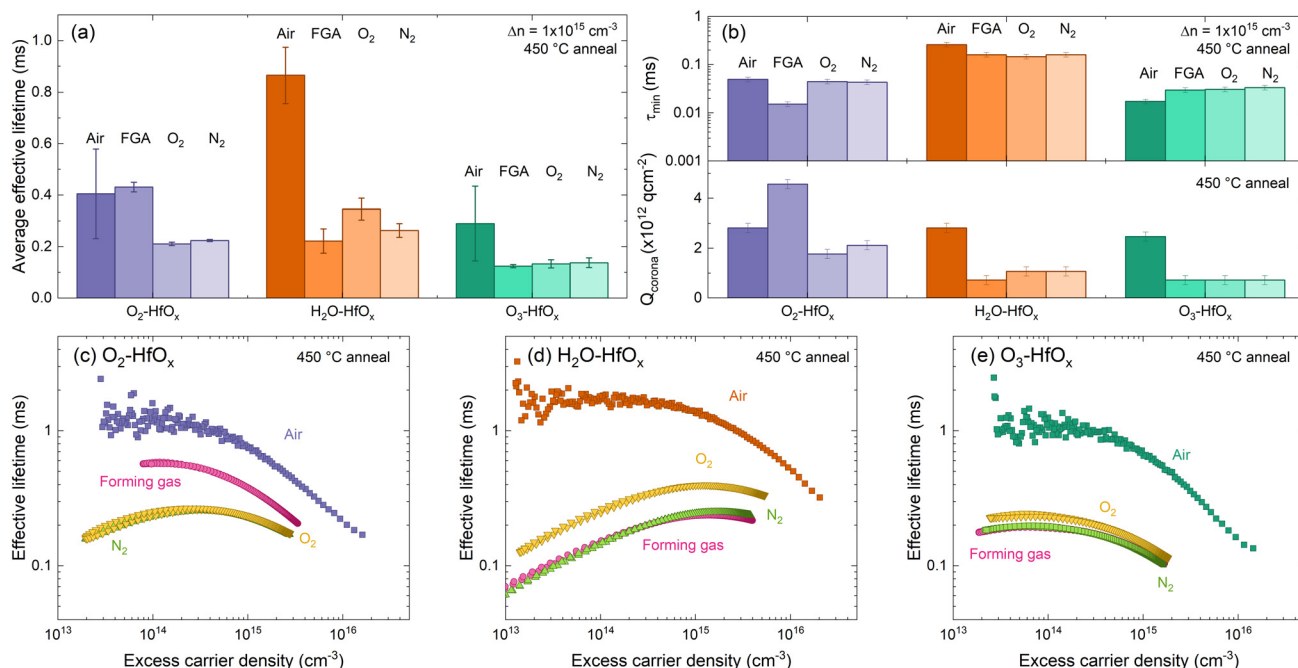


**Fig. 6** (a) Average effective lifetimes for  $\text{O}_2\text{-HfO}_x$  (purple),  $\text{H}_2\text{O-HfO}_x$  (orange) and  $\text{O}_3\text{-HfO}_x$  (green) after annealing in air, forming gas (FGA),  $\text{O}_2$  and  $\text{N}_2$  environments (dark to light shades) at 450 °C for 30 min. Error bars are the experienced variation between samples and plotted effective lifetimes were extracted at  $1 \times 10^{15} \text{ cm}^{-3}$ . Duplicate samples of  $\text{O}_2\text{-HfO}_x$ ,  $\text{H}_2\text{O-HfO}_x$  and  $\text{O}_3\text{-HfO}_x$  were measured per annealing condition. (b)  $\tau_{\text{min}}$  (top)  $Q_{\text{corona}}$  (bottom) for  $\text{O}_2\text{-HfO}_x$  (purple),  $\text{H}_2\text{O-HfO}_x$  (orange) and  $\text{O}_3\text{-HfO}_x$  (green) after annealing in air, forming gas,  $\text{O}_2$  and  $\text{N}_2$  environments (dark to light shades) at 450 °C for 30 min. In both cases, the shaded region corresponds to the relative uncertainty of the measurement (11% in the case of  $\tau_{\text{min}}$ ,<sup>46</sup> and  $Q_{\text{corona}}$  of  $1.85 \times 10^{11} \text{ q cm}^{-2}$ , 50% of  $Q_{\text{corona}}$  deposited in each step in the bottom case). Optimum injection-dependent effective lifetimes of (c)  $\text{O}_2\text{-HfO}_x$ , (d)  $\text{H}_2\text{O-HfO}_x$ , and (e)  $\text{O}_3\text{-HfO}_x$  after annealing in air, forming gas (pink),  $\text{O}_2$  (yellow) and  $\text{N}_2$  (green) environments at 450 °C for 30 min.

but there is only a marginal difference between this and the other values. Above this temperature, there is a monotonic decrease in  $\tau_{\min}$ . The 'activation' anneal appears to mainly impact fixed charge levels, with a minor increase in chemical passivation, although beyond  $\sim 400$  °C increasing fixed charge further is counterbalanced by reduced chemical passivation.  $\text{O}_2\text{-HfO}_x$  has intermediary behaviour. Like for  $\text{O}_3\text{-HfO}_x$ ,  $Q_{\text{fixed}}$  is initially low, but improves with annealing.

With annealing at 425–500 °C  $Q_{\text{fixed}}$  is similar, akin to  $\text{H}_2\text{O-HfO}_x$ .  $\text{O}_2\text{-HfO}_x$  also exhibits  $\tau_{\min}$  between that of  $\text{H}_2\text{O-HfO}_x$  and  $\text{O}_3\text{-HfO}_x$  at all temperatures studied. The difference in  $\tau_{\min}$  between  $\text{H}_2\text{O-HfO}_x$  and  $\text{O}_3\text{-HfO}_x$ , with  $\text{O}_2\text{-HfO}_x$  falling in between, implies different degrees of chemical passivation of the Si/HfO<sub>x</sub> interface. The lower quality chemical passivation with  $\text{O}_2\text{-HfO}_x$  and  $\text{O}_3\text{-HfO}_x$  may arise from interfacial damage accrued during deposition from the reactive plasma and ozone radicals, as suggested by Dingemans *et al.*<sup>45</sup>

An alternative could be that the interfaces grow similarly but that  $\text{H}_2\text{O-HfO}_x$  is inherently improved by the presence of hydrogen in the  $\text{H}_2\text{O}$  precursor,<sup>11</sup> with the hydrogen content of ALD-grown films reported to be greater for those grown with a  $\text{H}_2\text{O}$  co-reactant *versus*  $\text{O}_2$  plasma.<sup>16</sup> Hydrogen is well-known to passivate interfacial defects and may be provided *in situ* from the co-reactant. It is important to note that the co-reactant is not the sole source of hydrogen in the deposition process. The hafnium precursor TDMAH is also a potential hydrogen source, *cf.*, trimethylaluminium (TMA), a common  $\text{Al}_2\text{O}_3$  ALD precursor, which contributes to the overall hydrogen content of the film.<sup>47</sup> The good passivation quality observed for  $\text{H}_2\text{O-HfO}_x$  relative to  $\text{O}_3\text{-HfO}_x$  and  $\text{O}_2\text{-HfO}_x$  without any annealing step (shown in Fig. 3), demonstrates that the difference in passivation is linked to the deposition process, rather than any post-treatment. At low ( $\sim 350$  °C) annealing temperatures,  $\text{H}_2\text{O-HfO}_x$  reaches  $Q_{\text{fixed}}$  of order  $-10^{12}$  q cm<sup>-2</sup>, whilst the other HfO<sub>x</sub> films require higher annealing temperature to reach the same level.  $\text{H}_2\text{O-HfO}_x$  and  $\text{O}_2\text{-HfO}_x$  appear to have greater  $Q_{\text{fixed}}$  than  $\text{O}_3\text{-HfO}_x$  at most annealing temperatures.

The origin of the fixed charges in HfO<sub>x</sub> are debated, although it is thought to be linked to oxygen sites/vacancies, with positive charges attributed to oxygen vacancies or under-coordinated oxygen sites,<sup>8,13</sup> while negative charges are attributed to oxygen interstitials and hafnium vacancies.<sup>37</sup> The XPS data presented in Fig. 1, collected from HfO<sub>x</sub> annealed at 450 °C demonstrates that at the film surface,  $\text{O}_3\text{-HfO}_x$  is more oxygen-rich than  $\text{H}_2\text{O-HfO}_x$  and  $\text{O}_2\text{-HfO}_x$ , but at the dielectric/Si interface this is reversed.  $\text{H}_2\text{O-HfO}_x$  and  $\text{O}_2\text{-HfO}_x$  films annealed at 450 °C have both higher interfacial oxygen concentrations and interfacial charge density than comparable  $\text{O}_3\text{-HfO}_x$ , suggesting the negative charge observed in this case may be related to oxygen interstitials/hafnium vacancies.

To assess whether the improved passivation with  $\text{H}_2\text{O-HfO}_x$  was related to additional hydrogenation (beyond that potentially provided by the metal precursor) provided from

the  $\text{H}_2\text{O}$  co-reactant, forming gas anneals were performed, as these have been reported to provide additional interface hydrogenation.<sup>48</sup> Duplicate samples of  $\text{O}_2\text{-HfO}_x$ ,  $\text{O}_3\text{-HfO}_x$  and  $\text{H}_2\text{O-HfO}_x$  were annealed in different environments, namely forming gas ( $\text{H}_2/\text{N}_2$ ),  $\text{N}_2$  and  $\text{O}_2$ , for 30 min in a tube furnace at 450 °C.

Comparing the average effective lifetimes extracted at  $1 \times 10^{15}$  cm<sup>-3</sup> for each film type and annealing environment, shown in Fig. 6(a), yields some insight. For each film type, the highest passivation quality is generally achieved with annealing in an air environment (consistent with both our prior work<sup>6</sup> and recent reports<sup>13,49</sup>), although for  $\text{O}_2\text{-HfO}_x$  similar passivation quality is achieved for air as for a forming gas environment. For all co-reactants, similar passivation is obtained when annealing in either an  $\text{O}_2$  or  $\text{N}_2$  environment (lower than that obtained with annealing in an air environment), consistent with our prior work on  $\text{O}_2\text{-HfO}_x$ .<sup>6</sup> Of all films studied, the most amenable to forming gas annealing is  $\text{O}_2\text{-HfO}_x$ , with this approach offering no advantage for  $\text{H}_2\text{O-HfO}_x$  and  $\text{O}_3\text{-HfO}_x$ .

Focusing on extracted lifetimes at a single injected minority charge density – such as  $1 \times 10^{15}$  cm<sup>-3</sup> – only tells part of the story. More information can be gleaned from the injection dependent lifetime curves.<sup>50</sup> Curves measured on the samples annealed in different environments are shown in Fig. 6(b). The gradient of  $\text{H}_2\text{O-HfO}_x$  lifetime curves annealed in forming gas,  $\text{O}_2$  and  $\text{N}_2$  suggest a low field effect contribution relative to chemical effect. To extract more information around the relative effects of chemical and field effect passivation, corona charging was used. As all samples exhibited the behaviour shown in Fig. 5(a) on corona charging, it is clear that the annealing environment does not affect film charge polarity, with negative charges exhibited in each case.

In air, annealing at 450 °C resulted in similar levels of field effect passivation (determined from  $-Q_{\text{corona}}$ ) but different levels of chemical effect (determined from  $\tau_{\min}$ ) passivation, with chemical passivation increasing in the order  $\text{H}_2\text{O-HfO}_x > \text{O}_2\text{-HfO}_x > \text{O}_3\text{-HfO}_x$ . This trend in chemical passivation is maintained with changing annealing environment, as shown in Fig. 6(c), but field effect passivation differs considerably.

Between annealing environments there is minimal variation in  $\tau_{\min}$  for each film type. For  $\text{O}_2\text{-HfO}_x$  and  $\text{H}_2\text{O-HfO}_x$ , changing annealing environment away from air reduces  $\tau_{\min}$ , whilst the converse is true for  $\text{O}_3\text{-HfO}_x$ , for which there is increased chemical passivation.

For all film types, the highest levels of field effect passivation ( $\sim 3 \times 10^{12}$  q cm<sup>-2</sup>) were achieved with annealing in air, excepting  $\text{O}_2\text{-HfO}_x$ , for which greater field effect passivation ( $\sim 4.5 \times 10^{12}$  q cm<sup>-2</sup>) was observed. In all other cases,  $Q_{\text{corona}}$  reduced considerably relative to that obtained after annealing in air.

The data presented in Fig. 5 demonstrated that ALD co-reactant does not influence charge polarity but does influence charge magnitude and chemical passivation. The



data shown in Fig. 6 demonstrates that that the same can be said of annealing environment, which has a considerable impact on resulting passivation quality. It should be noted though, that different furnaces were used for annealing in air *versus* the defined environments, although the same temperature and process duration were targeted.

## Experimental

### Film preparation

Substrates for effective charge carrier lifetime and Kelvin probe measurements were high quality,  $\sim 150\ \mu\text{m}$  thick, (100) orientation, monocrystalline  $5\ \Omega\ \text{cm}$  resistivity, phosphorus doped n-type Czochralski-grown silicon wafers with a chemically etched surface finish. Samples were prepared following a previously reported chemical cleaning and etching procedure,<sup>51</sup> based on the 'RCA' standard clean. This procedure has previously been shown to enable good quality  $\text{HfO}_x$  passivation.<sup>11,52</sup> The final step in the cleaning process (immersion in 2% HF for 60 s) was modified to immersion in 1% HF/1% HCl for 5 min with no subsequent water rinse, as this has been found to improve final passivation quality.<sup>53</sup> Substrates for film thickness measurements were  $\sim 725\ \mu\text{m}$  thick, mirror polished (100) wafers, and underwent an identical cleaning process, with the omission of etching.<sup>53</sup>

Coatings were grown *via* ALD using a Veeco Fiji G2 system (with plasma-enhanced or thermal capability) with an external load lock.  $\text{HfO}_x$  films were deposited on both sides of each wafer at  $200\ ^\circ\text{C}$  from a tetrakis(dimethylamido) hafnium (TDMAH) precursor (Pegasus Ltd.). 200 ALD cycles were used for each film with varying co-reactants – either  $\text{O}_2$  plasma, ozone ( $\text{O}_3$ ) or water ( $\text{H}_2\text{O}$ ). In all cases, the precursor was heated to  $75\ ^\circ\text{C}$  and Ar was used as an inert carrier gas. Relevant deposition parameters are summarised in Table 1.  $\text{O}_3$  is generated prior to deposition from flowing  $\text{O}_2$  *via* a generator within the Fiji G2 system.

A post-deposition anneal in air was performed for 30 min in a quartz tube furnace at temperatures between  $350$ – $600\ ^\circ\text{C}$ , unless otherwise specified. Samples annealed in different environments (forming gas,  $\text{O}_2$ ,  $\text{N}_2$ ) were annealed in a sintering furnace under a gas flow of 1 slm at  $450\ ^\circ\text{C}$  for 30 min.

### Safety considerations

Dilute HF is used in this work as part of a standard industrial silicon cleaning process. It is important to note that HF is

corrosive and toxic,<sup>55</sup> and must be handled only by those trained in HF handling, hazards, and spill response. Exposure to HF and its fumes, even small quantities, can be fatal. HF work should be conducted in a well-ventilated fume hood with appropriate personal protective equipment: face shield, apron, and HF-resistant gloves. HF etches glass, so must be contained in HF-compatible beakers.

The reagents used within the ALD deposition also introduce their own hazards – TDMAH (used as a hafnium precursor) is flammable, pyrophoric and corrosive,<sup>56</sup> while ozone (used as a co-reagent) has to be kept at low concentrations (ideally controlled with an ozone generator and sensor), lest explosive decomposition reactions occur.<sup>57</sup>

### Characterisation

**Spectral reflectance.** Spectral analysis was used to determine film thicknesses and resultant the growth rate of  $\text{HfO}_x$  using a Filmetrics F40-UV microscope, calibrated with a  $\text{SiO}_2/\text{Si}$  thickness standard. The F40-UV has a relative uncertainty of  $\pm 1\ \text{nm}$ .<sup>58</sup> Average thickness was determined from five points randomly distributed across the sample. Refractive indices as a function of wavelength were also determined from the same five points and averaged to produce a single spectrum.

**X-ray photoelectron spectroscopy (XPS).** XPS was performed at the Photoemission Research Technology Platform at the University of Warwick using a Kratos Axis Ultra DLD spectrometer. Samples were mounted on a non-magnetic, stainless-steel bar using electrically conductive carbon tape. The XPS spectrometer base pressure was  $\sim 1 \times 10^{-10}$  mbar, and samples were pumped to  $< 1 \times 10^{-6}$  mbar in the load lock before transfer, and then measured under a chamber pressure  $< 1 \times 10^{-9}$  mbar. XPS measurements were performed using a monochromated Al  $K\alpha$  X-ray ( $1.487\ \text{keV}$ ) source. Measurements were conducted at room temperature using a charge neutraliser and at a take-off angle of  $90^\circ$  with respect to the sample surface. All XPS spectra were calibrated to the C 1s core level. Core level spectra were recorded from an analysis area of  $300 \times 700\ \mu\text{m}$  by using a pass energy of  $40\ \text{eV}$  (resolution approx.  $0.7\ \text{eV}$ ).

Fitting procedures to extract peak positions and relative stoichiometries were performed using the Casa XPS software suite, linear backgrounds, and mixed Gaussian–Lorentzian (Voigt) line shapes. These were fitted and corrected using their corresponding sensitivity factors, considering the photoelectron mean free paths and photoionization cross sections of these core levels. The spectrometer work function and binding energy scale were calibrated using the Fermi edge and Ag  $3d_{5/2}$  peak from a clean polycrystalline Ag sample measured prior to the experiments.

Depth profiles were collected by etching samples *via* monoatomic  $\text{Ar}^+$  sputtering for a total duration of 9200 s. To calibrate the milling rate, thickogram method was used, which determines film thickness based on the intensity and kinetic energy of overlayer and substrate peaks, sensitivity

**Table 1** Summary of relevant parameters from the ALD process for each co-reactant used with the TMDAH precursor<sup>54</sup>

Conditions	$\text{O}_2$ plasma	$\text{H}_2\text{O}$	$\text{O}_3$
Pulse duration (s)	0.25	0.25	0.25
Precursor purge duration (s)	5	10	10
Co-reactant pulse duration (s)	6	0.06	0.15
Co-reactant intensity (W)	300	—	—
Co-reactant purge duration (s)	5	10	15



factors (7.12 for the  $\text{HfO}_x$  overlayer and 0.772 for the Si substrate) and the attenuation length of photoelectrons in overlayer (2.17 nm).<sup>30–32</sup> Thicknesses calculated using this method have an estimated uncertainty of  $\pm 30\%$ , based on the uncertainty in the attenuation length,<sup>32</sup> peak energies, and intensities.<sup>59</sup> Relative atomic concentrations were determined from core level peaks (Hf 4f, O 1s, Si 2p) identified from survey scans at multiple milling depths. Subsequent high-resolution core level spectra were collected, on which fitting and chemical state analysis, supported by the NIST XPS database,<sup>35</sup> were used to investigate the chemical composition of the film.

**X-ray diffraction.** Grazing incidence XRD (GI-XRD) was carried out at the X-ray Diffraction Research Technology Platform using a third generation Panalytical Empyrean XRD diffractometer, equipped with multicore (iCore, iCore) optics and a Pixel3D detector under  $\text{Cu K}\alpha_{1/2}$  radiation. The sample surface was aligned to the direct beam to ensure that it was at the centre of rotation of the goniometer, and the incident angle was set to  $0.5^\circ$ .  $2\theta$  measurements were made in the range of  $15\text{--}70^\circ 2\theta$ .

**Photoconductance decay.** Photoconductance decay lifetime measurements were performed at  $30^\circ\text{C}$  using a Sinton Instruments WCT-120PL lifetime tester (software version 5.74). Measurements were averaged over five measurements and were performed using the quick decaying (0.02 ms) flash mode, except for low effective lifetime samples ( $<200\ \mu\text{s}$  at  $\Delta n = 1 \times 10^{15}\ \text{cm}^{-3}$ ), which were measured using the slow-decaying (1.75 ms) flash.

Effective lifetime measurements made using the quick decaying and slow decaying flash are assumed to be accurate to  $\pm 8\%$  and  $\pm 11\%$ , respectively.<sup>46</sup> Effective lifetime measurements were made on samples following annealing in a forming gas,  $\text{O}_2$  and  $\text{N}_2$  environment using a spatially-resolved photoluminescence imaging modulum tool calibrated to carrier lifetimes, described in ref. 60. Measurements were made on  $5\ \text{cm} \times 5\ \text{cm}$  samples, considered sufficiently large to avoid strong impacts of edge recombination on the experiment.<sup>61</sup> Passivation quality was quantified in terms of SRV as:

$$\text{SRV} = \frac{W}{2} \left( \frac{1}{\tau_{\text{effective}}} - \frac{1}{\tau_{\text{bulk}}} \right) \quad (1)$$

where  $W$  is sample thickness, and  $\tau_{\text{bulk}}$  taken as the intrinsic (*i.e.*, radiative and Auger) limit using the parametrization of Niewelt *et al.*,<sup>40</sup> taking photon recycling into account by assuming planar sample surfaces. Assuming no extrinsic contribution to  $\tau_{\text{bulk}}$  means values of SRV are upper limits. Prior work using nominally identical  $\text{HfO}_x$ -coated Si substrates found these substrates to show no degradation of bulk lifetime at the annealing temperatures used herein.<sup>6</sup> Thus, we consider our results qualitatively comparable even if extrinsic recombination were present.  $J_{\text{os}}$  values, which have a relative uncertainty estimated to  $10\%$ ,<sup>62</sup> were determined *via* an automated fit to unsmoothed data evaluated using the 2-point derivation

method by the Sinton Lifetime Tester™ software (v.5.74). The fit region was centred around  $\Delta n = 1 \times 10^{15}\ \text{cm}^{-3}$ . A discussion on extracting  $J_{\text{os}}$  from this region can be found in ref. 63. Our samples are coated with identical dielectric films on both sides; hence we state single-side  $J_{\text{os}}$  values by dividing extracted  $J_{\text{os}}$  by 2.<sup>64</sup>

**Kelvin probe force microscopy.** Contact potential difference (CPD) measurements were made with a KP Technologies SKP5050 Kelvin Probe with a 2 mm gold-plated tip, based on the method of Baikie *et al.*<sup>65</sup> A Fiber-Lite DC-950 Quartz Tungsten Halide lamp was used for surface photovoltage (SPV) measurements. Surface photovoltage is defined as  $\text{CPD}_{\text{illumination}} - \text{CPD}_{\text{dark}}$ .

**Corona charging.** Corona charging was used to characterize the level of negative fixed charge in the dielectric films. Positive corona charging deposits extrinsic charge on the sample surface which offsets the built-in negative charges within the films. Eventually, successive corona charging counterbalances the intrinsic charge, with the quantity of deposited charge ( $Q_{\text{corona}}$ ) required to reach this point providing an estimation of  $Q_{\text{fixed}}$  in the film.<sup>42</sup> A custom-built corona charge apparatus, similar to that described by Bonilla *et al.*,<sup>66</sup> was used to deposit charge on the thin films. Samples were subjected to 3.5 V for 5 s on either side, which corresponds to deposited charge of  $\sim 3.7 \times 10^{11}\ \text{q cm}^{-2}$  per 5 s of corona charging. Following each corona charging treatment, effective lifetime was measured using the slow flash mode.

## Conclusions

We have studied ALD-grown hafnium oxide with three different co-reactants:  $\text{O}_2$  plasma,  $\text{O}_3$  and  $\text{H}_2\text{O}$ . Herein,  $\text{HfO}_x$  is deposited on n-type silicon from a tetrakis(dimethylamido) hafnium (TDMAH) precursor at  $200^\circ\text{C}$ , and characterised both in the as-deposited state and as a function of annealing temperature. The choice of co-reactant has a considerable impact on resultant film properties, with differences in crystallinity, composition, passivation quality, interfacial quality, and fixed charge magnitude. Depth profiling conducted with X-ray photoelectron spectroscopy reveals differences in composition between the  $\text{HfO}_x$  surface and the  $\text{HfO}_x/\text{Si}$  interface. We find that  $\text{H}_2\text{O}$ -based  $\text{HfO}_x$  gives rise to the best passivation quality, even at low annealing temperatures, as a result of high fixed negative charge levels ( $\sim 10^{12}\ \text{q cm}^{-2}$ ) and good chemical passivation. Neither the co-reactant choice nor annealing environment change the resulting charge polarity.

## Data availability

Data underpinning figures in this paper can be freely downloaded from <https://wrap.warwick.ac.uk/181742/>. Requests for additional data should be made directly to the corresponding authors.



## Author contributions

The research concept was devised by S. L. P. Experimental work, sample processing, characterization, and data analysis were largely conducted by S. L. P. with assistance from A. Y. and B. F. M. H. A. L. performed annealing under forming gas, nitrogen and oxygen environments. XPS data were collected and analysed by E. K. and M. W. N. E. G. developed the corona charging methodology and D. W. provided support with XRD data collection. S. L. P., E. K., T. N., N. E. G., and J. D. M. contributed to discussions and data analysis. The manuscript was written by S. L. P., with input from T. N., E. K., M. W., N. E. G. and J. D. M.

## Conflicts of interest

There are no conflicts to declare.

## Acknowledgements

Work was supported by the EPSRC Charged Oxide Inversion Layer (COIL) solar cells project (EP/V037749/1), and the Leverhulme Trust (RPG-2020-377). M. W. and D. W. acknowledge financial support from the EPSRC-funded Warwick Analytical Science Centre (EP/V007688/1). A. Y. was in receipt of an ISIS Facility Development Studentship from the Science and Technology Facilities Council. XPS and XRD analysis were conducted *via* the Warwick Photoemission and X-ray Diffraction Research Technology Platforms, respectively.

## References

- 1 R. S. Bonilla, B. Hoex, P. Hamer and P. R. Wilshaw, *Phys. Status Solidi A*, 2017, **214**, 1700293.
- 2 M. Leskelä and M. Ritala, *Angew. Chem., Int. Ed.*, 2003, **42**, 5548–5554.
- 3 S. M. George, *Chem. Rev.*, 2010, **110**, 111–131.
- 4 H. B. Profijt, S. E. Potts, M. C. M. van de Sanden and W. M. M. Kessels, *J. Vac. Sci. Technol., A*, 2011, **29**, 050801.
- 5 J. Hendrickson, A. Homyk, A. Scherer, T. Alasaarela, A. Säynätjoki, S. Honkanen, B. C. Richards, J.-Y. Kim, Y.-H. Lee, R. Gibson, M. Gehl, J. D. Olitzky, S. Zandbergen, H. M. Gibbs and G. Khitrova, in *Quantum Optics with Semiconductor Nanostructures*, ed. F. Jahnke, Woodhead Publishing, 2012, pp. 433–434.
- 6 A. Wratten, S. L. Pain, D. Walker, A. B. Renz, E. Khorani, N. E. Grant and J. D. Murphy, *IEEE J. Photovolt.*, 2023, **13**, 40–47.
- 7 N. E. Grant, S. L. Pain, E. Khorani, R. Jefferies, A. Wratten, S. McNab, Y. Han, R. Beanland, R. S. Bonilla and J. D. Murphy, *Appl. Surf. Sci.*, 2024, **645**, 158786.
- 8 F. Lin, B. Hoex, Y. H. Koh, J. Lin and A. G. Aberle, *Energ. Proc.*, 2012, **15**, 84–90.
- 9 F. Lin, B. Hoex, Y. H. Koh, J. Lin and A. G. Aberle, *ECS J. Solid State Sci. Technol.*, 2013, **2**, N11–N14.
- 10 J. Gope, Vandana, N. Batra, J. Panigrahi, R. Singh, K. K. Maurya, R. Srivastava and P. K. Singh, *Appl. Surf. Sci.*, 2015, **357**, 635–642.
- 11 X. Cheng, P. Repo, H. Halvard, A. P. Perros, E. S. Marstein, M. Di Sabatino and H. Savin, *IEEE J. Photovolt.*, 2017, **7**, 479–486.
- 12 J. Cui, Y. Wan, Y. Cui, Y. Chen, P. Verlinden and A. Cuevas, *Appl. Phys. Lett.*, 2017, **110**, 021602.
- 13 A. B. Gougam, B. Rajab and A. B. Afif, *Mater. Sci. Semicond. Process.*, 2019, **95**, 42–47.
- 14 V. Aubriet, K. Courouble, M. Gros-Jean and L. Borowik, *Rev. Sci. Instrum.*, 2021, **92**, 083905.
- 15 B. Hoex, S. B. B. Heil, E. Langereis, M. C. M. van de Sanden and W. M. M. Kessels, *Appl. Phys. Lett.*, 2006, **89**, 042112.
- 16 G. Dingemans and W. M. M. Kessels, *J. Vac. Sci. Technol., A*, 2012, **30**, 040802.
- 17 E. Khorani, C. Messmer, S. L. Pain, T. Niewelt, B. Healy, A. Wratten, M. Walker, N. E. Grant and J. D. Murphy, *IEEE J. Photovolt.*, 2023, **13**, 682–690.
- 18 A. Wratten, S. L. Pain, A. Yadav, E. Khorani, T. Niewelt, L. Black, G. Bartholazzi, D. Walker, N. E. Grant and J. D. Murphy, *Sol. Energy Mater. Sol. Cells*, 2023, **259**, 112457.
- 19 S. L. Pain, E. Khorani, T. Niewelt, A. Wratten, G. J. P. Fajardo, B. Winfield, R. S. Bonilla, M. Walker, L. F. J. Piper, N. E. Grant and J. D. Murphy, *Adv. Mater. Interfaces*, 2022, **9**, 2201339.
- 20 H. Mulaosmanovic, E. T. Breyer, S. Dünkler, S. Beyer, T. Mikolajick and S. Slesazek, *Nanotechnology*, 2021, **32**, 502002.
- 21 M. Pešić, F. P. G. Fengler, L. Larcher, A. Padovani, T. Schenk, E. D. Grimley, X. Sang, J. M. LeBeau, S. Slesazek, U. Schroeder and T. Mikolajick, *Adv. Funct. Mater.*, 2016, **26**, 4601–4612.
- 22 A. Wratten, B. F. M. Healy, D. Walker, E. Khorani, N. E. Grant and J. D. Murphy, *AIP Adv.*, 2023, **13**, 065113.
- 23 C. Richter, T. Schenk, U. Schroeder and T. Mikolajick, *J. Vac. Sci. Technol., A*, 2014, **32**, 01A117.
- 24 H. B. Park, M. Cho, J. Park, S. W. Lee, C. S. Hwang, J.-P. Jim, J.-H. Lee, N.-I. Lee, H.-K. Kang, J.-C. Lee and S.-J. Oh, *J. Appl. Phys.*, 2003, **94**, 3641–3647.
- 25 R. Sreenivasan, P. C. McIntyre, H. Kim and K. C. Saraswat, *Appl. Phys. Lett.*, 2006, **89**, 112903.
- 26 M. Dalberth, M. Sowa, E. Deguns, R. Bhatia, A. Bertuch, G. Liu, G. Sundaram and J. Becker, *ECS Meeting Abstracts*, 2010, **MA2010-02**, 1451.
- 27 S. Tomer, M. Devi, A. Kumar, S. Laxmi, C. M. S. Rauthan and Vandana, *IEEE J. Photovolt.*, 2020, **10**, 1614–1623.
- 28 J.-W. Park, D.-K. Lee, D. Lim, H. Lee and S.-H. Choi, *J. Appl. Phys.*, 2008, **104**, 033521.
- 29 B.-O. Cho, J. P. Chang, J.-H. Min, S. H. Moon, Y. W. Kim and I. Levin, *J. Appl. Phys.*, 2003, **93**, 745–749.
- 30 S. Tougaard, *QUASES-IMFP-TPP2MM (3.0)*, 2016.
- 31 S. Tanuma, C. J. Powell and D. R. Penn, *Surf. Interface Anal.*, 1994, **21**, 165–176.
- 32 P. J. Cumpson, *Surf. Interface Anal.*, 2000, **29**, 403–406.



- 33 C. E. Curtis, L. M. Doney and J. R. Johnson, *J. Am. Ceram. Soc.*, 1954, **37**, 458–465.
- 34 I. Zrinski, C. C. Mardare, L.-I. Jinga, J. P. Kollender, G. Socol, A. W. Hassel and A. I. Mardare, *Appl. Surf. Sci.*, 2021, **548**, 149093.
- 35 National Institute of Standards and Technology, NIST X-ray Photoelectron Spectroscopy Database 20, National Institute of Standards and Technology, Maryland, USA, 4.1 edn, 2000.
- 36 S. Tomer, M. Devi, A. Kumar, S. Laxmi, S. Satapathy, K. K. Maurya, P. Singh, P. Pathi and Vandana, *IEEE J. Photovolt.*, 2023, **13**, 691–698.
- 37 R. Singh, Vandana, J. Panigrahi and P. K. Singh, *RSC Adv.*, 2016, **100**, 97720–97727.
- 38 L. Kronik and Y. Shapira, *Surf. Sci. Rep.*, 1999, **37**, 1–206.
- 39 R. S. Bonilla, *Mater. Res. Express*, 2022, **9**, 085901.
- 40 T. Niewelt, B. Steinhäuser, A. Richter, B. Veith-Wolf, A. Fell, B. Hammann, N. E. Grant, L. Black, J. Tan, A. Youssef, J. D. Murphy, J. Schmidt, M. C. Schubert and S. W. Glunz, *Sol. Energy Mater. Sol. Cells*, 2022, **235**, 111467.
- 41 R. J. Hamers and K. Markert, *Phys. Rev. Lett.*, 1990, **64**, 1051–1054.
- 42 B. Hoex, J. Schmidt, M. C. M. van de Sanden and W. M. M. Kessels, presented in part at the *33rd IEEE Photovoltaic Specialist Conference (PVSEC 2008)*, California, USA, 2008.
- 43 Y. Zhao, C. Zhou, X. Zhang, P. Zhang, Y. Dou, W. Wang, X. Cao, B. Wang, Y. Tang and S. Zhou, *Nanoscale Res. Lett.*, 2013, **8**, 114.
- 44 R. S. Bonilla, C. Reichel, M. Hermle and P. R. Wilshaw, *Phys. Status Solidi RRL*, 2017, **11**, 1600307.
- 45 G. Dingemans, N. M. Terlinden, D. Pierreux, H. B. Profijt, M. C. M. van De Sanden and W. M. M. Kessels, *Electrochem. Solid-State Lett.*, 2010, **14**, H1.
- 46 A. L. Blum, J. S. Swirhun, R. A. Sinton, F. Yan, S. Herasimenka, T. Roth, K. Lauer, J. Haunschild, B. Lim, K. Bothe, Z. Hameiri, B. Seipel, R. Xiong, M. Dhamrin and J. D. Murphy, *IEEE J. Photovolt.*, 2014, **4**, 525–531.
- 47 C. Guerra-Núñez, M. Döbeli, J. Michler and I. Utke, *Chem. Mater.*, 2017, **29**, 8690–8703.
- 48 J.-I. Polzin, B. Hammann, T. Niewelt, W. Kwapil, M. Hermle and F. Feldmann, *Sol. Energy Mater. Sol. Cells*, 2021, **230**, 111267.
- 49 X.-Y. Zhang, J. Han, Y.-T. Wang, Y.-J. Ruan, W.-Y. Wu, D.-S. Wu, J. Zuo, F.-M. Lai, S.-Y. Lien and W.-Z. Zhu, *Sol. Energy Mater. Sol. Cells*, 2023, **257**, 112384.
- 50 L. E. Black, in *New perspectives on surface passivation: Understanding the Si-Al<sub>2</sub>O<sub>3</sub> interface*, Springer, 2016, ch. 2.6, p. 27.
- 51 N. E. Grant, P. P. Altermatt, T. Niewelt, R. Post, W. Kwapil, M. C. Schubert and J. D. Murphy, *Sol. RRL*, 2021, **5**, 2000754.
- 52 A. Wratten, *PhD thesis*, University of Warwick, 2023.
- 53 N. E. Grant, A. I. Pointon, R. Jefferies, D. Hiller, Y. Han, R. Beanland, M. Walker and J. D. Murphy, *Nanoscale*, 2020, **12**, 17332–17341.
- 54 Ultratech/Cambridge Nanotech, Fiji HfO<sub>2</sub> Thermal and Plasma, 2015.
- 55 Sigma Aldrich, MSDS - 339261, <https://www.sigmaaldrich.com/GB/en/sds/sigald/339261>, (accessed 25th October, 2023).
- 56 Sigma Aldrich, MSDS 455199 - Tetrakis(dimethylamido) hafnium(IV), <https://www.sigmaaldrich.com/GB/en/sds/aldrich/455199>, (accessed 16th November 2023).
- 57 H. Park, J. Park, S. Shin, G. Ham, H. Choi, S. Lee, N. Lee, S. Kwon, M. Bang, J. Lee, B. Kim and H. Jeon, *J. Vac. Sci. Technol., A*, 2018, **36**, 051509.
- 58 Filmetrics Inc, Operations Manual for the FILMETRICS F20 Thin-Film Analyzer, Filmetrics Inc., 7.3.2 edn., 2013.
- 59 R. Hesse, T. Chasse, P. Streubel and R. Szargan, *Surf. Interface Anal.*, 2004, **36**, 1373–1383.
- 60 H. Höffler, F. Schindler, A. Brand, R. Eberle, R. Post, A. Kessel, J. Greulich and M. C. Schubert, presented in part at the *37th European PV Solar Energy Conference and Exhibition*, 2020.
- 61 M. Kessler, T. Ohrdes, P. P. Altermatt and R. Brendel, *J. Appl. Phys.*, 2012, **111**, 054508.
- 62 D. E. Kane and R. M. Swanson, presented in part at the *18th IEEE Photovoltaic Specialists Conference*, Las Vegas, 1985.
- 63 B. Hammann, B. Steinhäuser, A. Fell, R. Post, T. Niewelt, W. Kwapil, A. Wolf, A. Richter, H. Höffler and M. C. Schubert, *IEEE J. Photovolt.*, 2023, **13**, 535–546.
- 64 D. Kang, H. C. Sio, J. Stuckelberger, D. Yan, S. P. Phang, R. Liu, T. N. Truong, T. Le, H. T. Nguyen, X. Zhang and D. Macdonald, *Progr. Photovolt.: Res. Appl.*, 2022, **30**, 970–980.
- 65 I. D. Baikie, S. Mackenzie, P. J. Z. Estrup and J. A. Meyer, *Rev. Sci. Instrum.*, 1991, **62**, 1326–1332.
- 66 R. S. Bonilla, C. Reichel, M. Hermle, P. Hamer and P. R. Wilshaw, *Appl. Surf. Sci.*, 2017, **412**, 657–667.

